

Introduction

InN and GaN can form an alloy in wurtzite-structure. The alloy on the Ga-rich side is the key component of blue light emitting devices. Early studies of InN films grown by the sputtering method have suggested a direct band gap of 2 eV. However, the recent optical characterizations of InN crystals grown by molecular-beam epitaxy (MBE) or metal-organic vapor phase epitaxy (MOCVD) showed that the real band-gap energy of InN is actually about 0.7 eV [1-5]. Hence, the gap energy of InGaN ternary alloys has been shown to cover a wide, continuous spectral range from the near infrared for InN to the near ultraviolet for GaN. This is the motivation that we study this material.

In fabrication of nitride-based devices, the strain relaxation in nitride materials is very important because the strain will influence device properties such as energy band gap, carrier lifetime, or induced piezoelectric field. Hence, the purpose of this thesis is to study the strain influence of InN nano-dots with different dot height, different growth temperature and cap GaN 35nm on InN dots by μ -Raman and X-ray diffraction.

There are four chapters in this thesis. In chapter 1, we briefly describe the InN structure, Raman scattering, X-ray diffraction and optical transitions of III-Nitride semiconductors. In chapter 2, we give the detail

of sample preparations and experiment setups. In chapter 3, we combine the X-ray diffraction and μ -Raman results to analyze the strain in InN epilayer and nano-dots with different growth conditions. Finally, in chapter 4, we summarize the experimental results of InN nano dots and give a conclusion.



Chapter 1 Theoretical Background

1.1 The Raman scattering

1.1.1 InN structure

As shown in Figure 1-1, InN can be formed into two structures: the hexagonal wurtzite (h-InN) and the cubic zinc-blende (c-InN). Since the wurtzite structure is the stable phase while the zinc blende structure is metastable, most of our studies concentrate on h-InN [6].

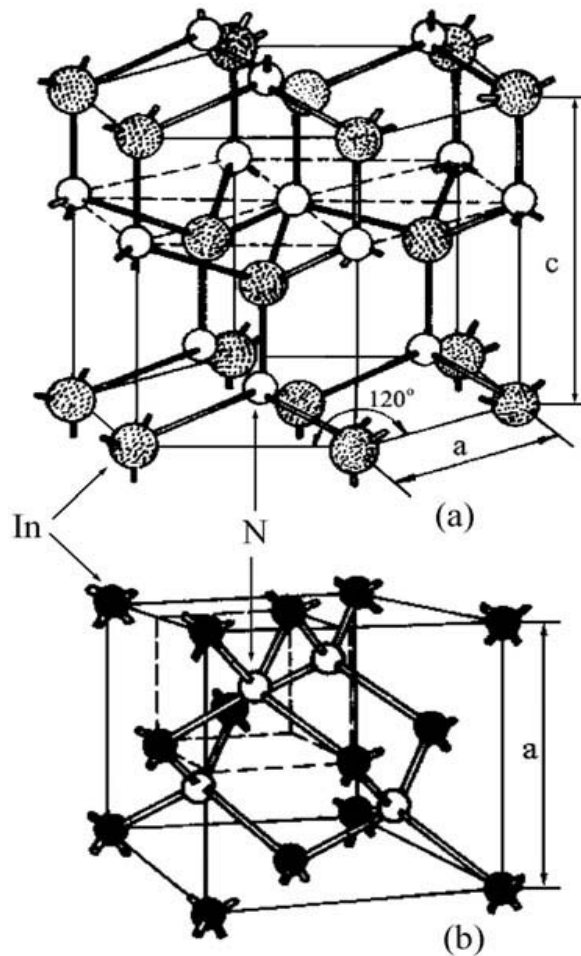


Figure 1-1. The structure of (a) wurtzite InN (h-InN) and (b) zinc blende InN (c-InN) [6].

Wurtzite-InN has four atoms per unit cell, i.e., two In–N atom pairs. Zinc-blende InN has two atoms per unit cell, i.e., one In–N atom pair. In both cases, one In atom is involved in a tetrahedron of N atom and vice versa. h-InN is different from c-InN only in the stacking order of In–N atom layers: h-InN is ABAB...type along the [0001] direction and c-InN is ABCABC...type along the [111] direction. Thus, the phonon structure of h-InN is similar to that of c-InN, i.e., the phonon dispersion along [0001] ($\Gamma \rightarrow A$ direction in Brillouin zone) in h-InN can be approximately obtained by folding the phonon dispersion along [111] ($\Gamma \rightarrow L$ direction) in c-InN.

1.1.2 Lattice vibrations of the wurtzite InN

The Raman scattering of phonons in crystals can be explained by the interactions of phonons and photons [7, 8]. An incident photon of frequency of ω_L interacts with phonons in crystals and then annihilates or generates a phonon of frequency ω_{ph} , so the frequency of the scattered photon is

$$\omega_S = \omega_L \pm \omega_{ph} \quad (1)$$

Regarding the wavevectors of the incident photon k_L , scattered photon k_S , and phonon q , they are related by

$$k_S = k_L \pm q \quad (2)$$

Equations (1) and (2) satisfy the conservation of energy and momentum, respectively, with “-” sign for the Stokes scattering and “+” sign for the

anti-Stokes scattering. The frequency difference of the scattered photon from the incident photon is called the Raman shift, which corresponds to the phonon frequency and is generally in the range of 50–1000 cm^{-1} . Lasers from near-infrared to near-ultraviolet ($k_L \approx 10^4 \text{ cm}^{-1}$) are usually employed in experiments; the maximum of the wavevector change during the scattering (i.e., the wavevector of the photon) is $2k_L$, which is much smaller than the Brillouin zone ($\sim 10^8 \text{ cm}^{-1}$). We can therefore conclude that only the phonons near the Brillouin zone center will contribute to the Raman scattering. The Raman scattering geometry is normally described as $\vec{k}_L (\vec{a}_L, \vec{a}_S) \vec{k}_S$, for incident direction (incident polarization, scattering polarization) scattering direction. For lattice vibrational modes, Raman spectra can be observed under the geometry configuration only when the scattering cross section is nonzero, according to the group theory selection rules. It is called the first-order Raman scattering when the scattering process involves only one phonon. Under proper conditions, one can observe the second-order scattering, i.e., two phonons are annihilated or generated at the same time or one phonon annihilated and another one generated. In this case, phonons away from the Γ point can contribute to the Raman scattering, so long as they satisfy equations (1) and (2). The Raman scattering cross section can be written as [9]

$$\frac{d\sigma}{d\Omega} = W \left| \vec{a}_S \cdot \vec{R} \cdot \vec{a}_L \right|^2 \quad (3)$$

where W is a constant and \vec{R} is the Raman tensor, which is related to the polarizability tensor χ_{ij} of the crystal.

Wurtzite-InN belongs to the C_{6v}^4 space group. Group theory predicts one A_1 , one E_1 , two E_2 , and two B_1 modes and the corresponding Raman tensors are as follows:

$$A_1(z) = \begin{vmatrix} a & 0 & 0 \\ 0 & a & 0 \\ 0 & 0 & b \end{vmatrix}, E_1(x) = \begin{vmatrix} 0 & 0 & c \\ 0 & 0 & 0 \\ c & 0 & 0 \end{vmatrix}, E_1(y) = \begin{vmatrix} 0 & 0 & 0 \\ 0 & 0 & c \\ 0 & c & 0 \end{vmatrix},$$

$$E_2 = \begin{vmatrix} 0 & d & 0 \\ d & -d & 0 \\ 0 & 0 & b \end{vmatrix}, B_1 = \begin{vmatrix} e & f & 0 \\ f & -e & 0 \\ 0 & 0 & 0 \end{vmatrix} \quad (5)$$

A_1 and E_1 are symmetric modes corresponding to the axial and planar vibrations, respectively. They split into longitudinal acoustic and optical (LA and LO) and transverse acoustic and optical (TA and TO), and the LO and TO branches can be activated both in the Raman and infrared spectra. E_2 and B_1 are non-polar modes and E_2 is only Raman active while B_1 mode is forbidden. Figure 1-2 gives the vibrational types of the atoms in the unit cell corresponding to these phonon modes, and E_2 and B_1 each have two modes marked '(high)' and '(low)' according to their frequencies. Therefore, the Raman active modes of h-InN are A_1 (LO), A_1 (TO), E_1 (LO),

E_1 (TO), E_2 (high) and E_2 (low). Table 1-1 shows the observable modes in different scattering geometry configurations based on group theory selection rules. Some modes of InN are reported in Table 1-2 [10].



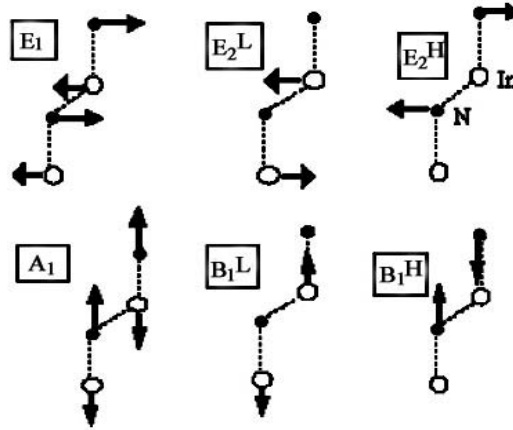


Figure 1-2. The atom vibration modes in wurtzite-InN with the c-axis upwards. The superscripts H and L represent the high and low frequency modes, respectively [6].

Geometry configuration	Active phonon modes
$x(y, y)\bar{x}$	$A_1(\text{TO}), E_2$
$x(z, z)\bar{x}$	$A_1(\text{TO})$
$x(z, y)\bar{x}$	$E_1(\text{TO})$
$x(y, z)y$	$E_1(\text{TO}), E_1(\text{LO})$
$x(y, y)z$	E_2
$z(x, y)\bar{z}$	E_2
$z(x, x)\bar{z}$	$A_1(\text{LO}), E_2$

Table 1-1. Active phonon modes in wurtzite -InN under different geometry configurations (the z direction is defined parallel to the c-axis of wurtzite -InN).

E_2 (low)	B_1 (low)	LOPC (low)	E_1 (TO)	A_1 (TO)	E_2 (high)	B_1 (high)	E_1 (LO)	A_1 (LO)
Experimental								
...	495	596
...	491	590
...	475	446	488	574
...	491	590
87	200	...	476	480	488	540	570	580
87	...	450	476	447	488	...	593	586
87	476	447	488	...	593	586
82	488	588
88	440	490	590
87	...	441	491	588
...	...	440	488	587
88	...	450	490	590
88	...	440	489	589
88	491	589
Theoretical								
104	270	...	472	440	483	530
93	202	...	470	443	492	568	605	589

Table 1-2. Raman data reported for hexagonal InN [10].

1.2 The X-ray diffraction

X-ray diffraction (XRD) technique is a non-destructive method for determining crystalline structure. This technique can be used for measuring the lattice mismatch between an epitaxial layer and the substrate, and thus for assessing the crystalline quality of epilayers. XRD is interpreted by two successive Bragg reflections from two adjacent lattice crystal planes, as shown in the scheme of Figure 1-3.

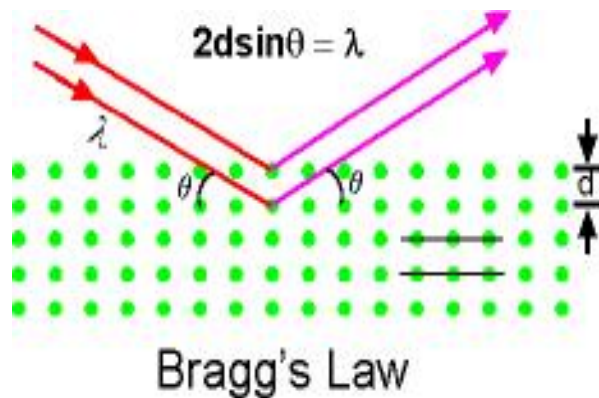


Figure 1-3. The XRD scheme

The condition for constructive interference is given by Bragg's law:

$$2d_{hkl} \sin \theta_B = n\lambda \quad (1)$$

where d_{hkl} is the reciprocal lattice spacing and can be expressed by

$$d_{hkl} = \frac{c}{\sqrt{h^2 + k^2 + l^2}} \quad (2)$$

where c is the crystal lattice constant; (h, k, l) is known as the Miller indices of the plane. θ_B is the incident angle, n is an integer representing the diffraction order and λ is the wavelength of the incident radiation

(0.154056nm for Cu K_{α} line). For a fixed incident X-ray wavelength λ , each crystalline solid has a characteristic X-ray diffraction pattern associated with it, which yields an accurate information on its crystal and lattice spacing. Hence, we can compare the crystal lattice constants of different InN dots to the strain free InN crystal lattice constant and calculate the residual strain in our samples.



1.3 Photoluminescence

Photoluminescence (PL) is one of the most useful optical methods for semiconductor characterizations. It is powerful and sensitive to find impurities and defects in semiconductors, which affect material quality and device performance. The full width at half maximum (FWHM) of the PL peaks is an indication of sample crystalline quality. When the incident laser photon energy is absorbed, an electron may be excited from the valence band (VB) to the conduction band (CB) to form an electron-hole pair for later recombination. Beside non-radiative (NR) transitions there are different ways to recombine electron-hole pairs that are called radiative recombination. Some fundamental radiative recombination and non-radiative transitions in semiconductor are shown in Figure 1-4.

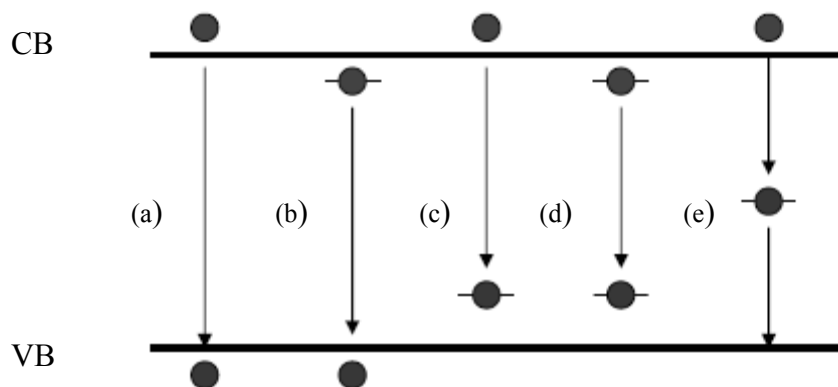


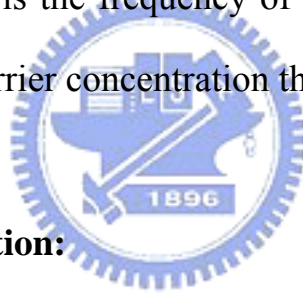
Figure1-4 Some fundamental transitions in semiconductor (a) band to band transition (b) donor to hole transition (c) electron to acceptor transition (d) donor to acceptor transition (e) non-radiative transition

(I) Band-to-band transition:

Band-to-band transition involves free electrons and holes between the conduction and valence bands. Such transition usually occurs in direct-gap material, such as III-V compounds, with conservation of momentum. The total e-h recombination rate is given by

$$R = \int R(h\nu)d(h\nu) \approx np \quad (1)$$

where n , p is the electron and hole concentration, respectively, h is the Planck's constant, ν is the frequency of the emitted photon. It indicates that the higher free carrier concentration the higher recombination rate.



(II) Free-to-bound transition:

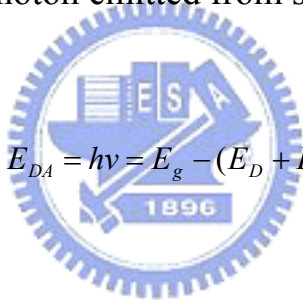
Transition between intrinsic band and impurity state, the so-called free-to-bound transition, may occur between impurity and one of the bands (e.g. the conduction band to acceptor or donor to the valence band) with momentum conservation even in indirect gap materials. Because of the small energies involved, phonon emission offers an effective competition route so that radiative efficiency is low. Transition of this type occurs close to the fundamental band gap and has been observed in many semiconductors.

(III) Donor-acceptor pairs (DAP) recombination:

Transition between donors and acceptors could take place by optical excitation, in which electrons and holes are trapped at D^+ and A^- sites to produce neutral D^0 and A^0 centers. In returning to equilibrium, some of the electrons on the neutral donors will recombine radiatively with holes on the neutral acceptors. It can be represented by the reaction.



The energy E_{DA} of a photon emitted from such a transition would be


$$E_{DA} = h\nu = E_g - (E_D + E_A) + \frac{Q^2}{\epsilon R_{DA}} \quad (3)$$

where E_D and E_A are the binding energies of donor and acceptor, respectively, Q is the elementary charge, ϵ is the dielectric constant of the material, and R_{DA} is the effective donor acceptor separation.

(IV) Non-radiative transition:

Several possible mechanisms leading to non-radiative transitions, competing with the radiative ones, and adversely affecting the luminescence efficiency, can be described as follows,

(i) Generation of phonons due to thermal vibrations.

(ii) Recombination at surface states, dislocation, grain boundaries, pores etc., by losing the excess energy through step-wise transitions, so called cascade-process, by emitting one single phonon in each step, between narrowly spaced levels existing throughout the forbidden energy gap in crystal joining the conduction and valence bands.

(iii) All defects site may not act as recombination centers to allow the carriers to recombine non-radiatively.

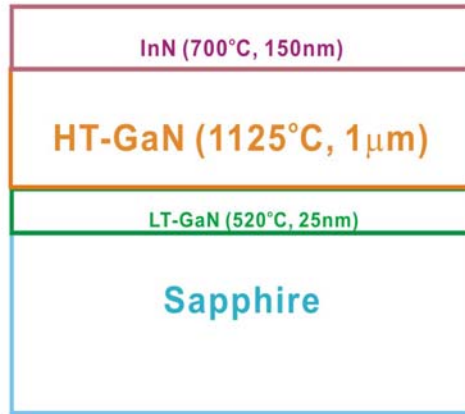
(iv) Auger process, in which the energy lost by the capture carrier excites another nearby carrier in the crystal, may give rise to energy loss non-radiatively. The other carrier can return to a lower energy state by multiple phonon emission.



Chapter 2 Experiments

2.1 Sample Preparation

Our InN samples were grown by Metalorganic Chemical Vapor Deposition System at the “Chung Shan Institute of Science and Technology”. The schematic structure of InN samples is shown in Figure 2-1-1. They were grown on (0002) sapphire by using Trimethylgallium (TMGa), Trimethylindium (TMIn), Ammonia (NH₃) as the Ga, In, N sources and the V/III ratio is 15000, the high-purity N₂ as the carrier gas and with the buffer layer of GaN deposited at temperatures 1125°C and 520°C using two-step process. The thickness of these buffer layers is 1μm and 25 nm, respectively. The different InN dot samples were obtained by changing the duration of growth cycles (20sec/cycles, 15sec/cycles, 10 sec/cycles). They have different dot height 28 nm, 19 nm 14 nm respectively as measured by AFM in Figure 2-1-2. We also deposited InN samples with similar dot heights but at different growth temperatures of 625°C, 650°C and 700°C. We will study the dot height and growth temperature and capping effects (35μm GaN) on the structure and optical properties of InN.



(a)

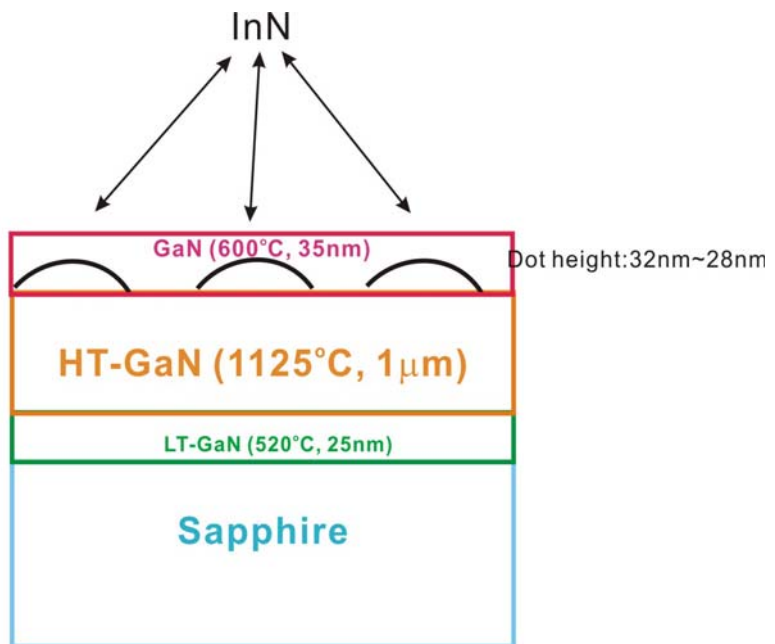
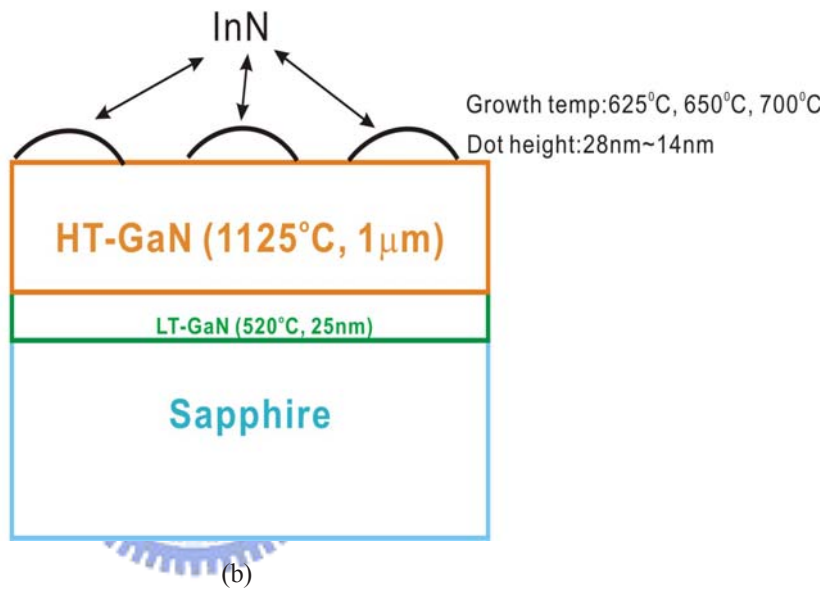
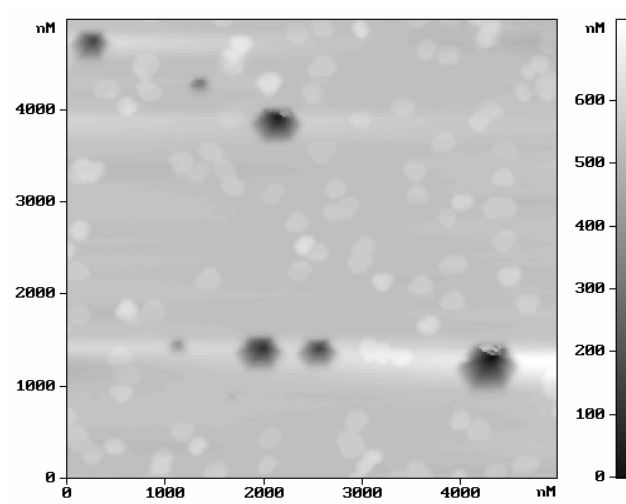
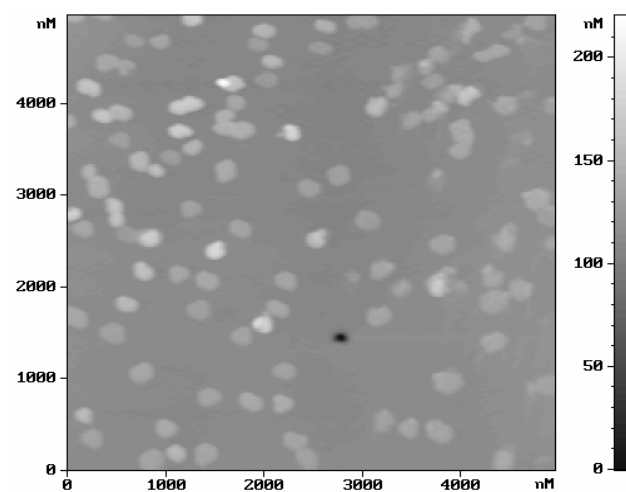


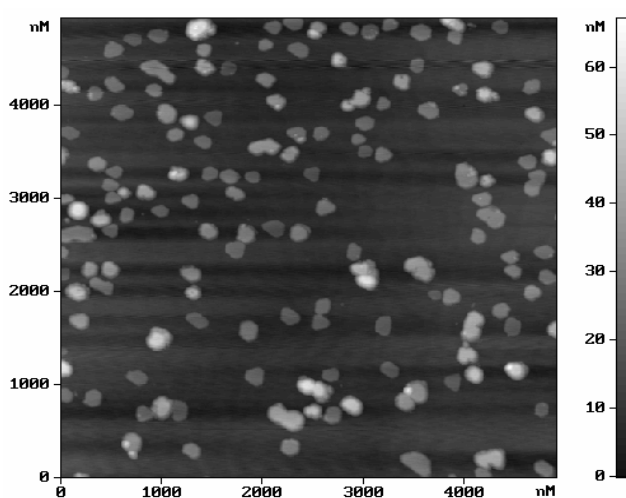
Figure 2-1-1. Sample structures of InN (a) epilayer, (b) dot, (c) dot with capping



(a)



(b)



(c)

Figure 2-1-2. The height of InN nano-dots with (a) 20sec/cycles(28nm)(b) 15sec/cycles(19nm) (c) 10sec/cycles(14nm) grown at 700°C

2.2 μ -Raman system

The Micro-Raman system as shown in Figure 2-2-1 consists of a Raman spectrometer (Jobin Yvon U-1000), a TE cooled CCD detector (Princeton Instruments PIXIS 100), a microscope (Olympus BX40) and an Ar⁺ laser source (Spectra-Physics stabilite 2017). The laser beam is directed by the mirror into the system and then reflected by a notch filter through the 100X objective lens (N.A. =0.9) and focused on the sample with a spot size about 2 μm in diameter. The Raman signals from the sample and the laser signals reflected by the sample were both collected by the objective lens. The Raman signals passing through the notch filter are coupled into the fiber and guided into the spectrometer for dispersion. This Raman spectrometer is equipped with double gratings (1800g/mm), that achieves a spectral resolution of $\sim 0.9 \text{ cm}^{-1}$ with the slit opening at 150 μm . Finally, the dispersed Raman signals will be collected by the CCD detector for spectral analysis.

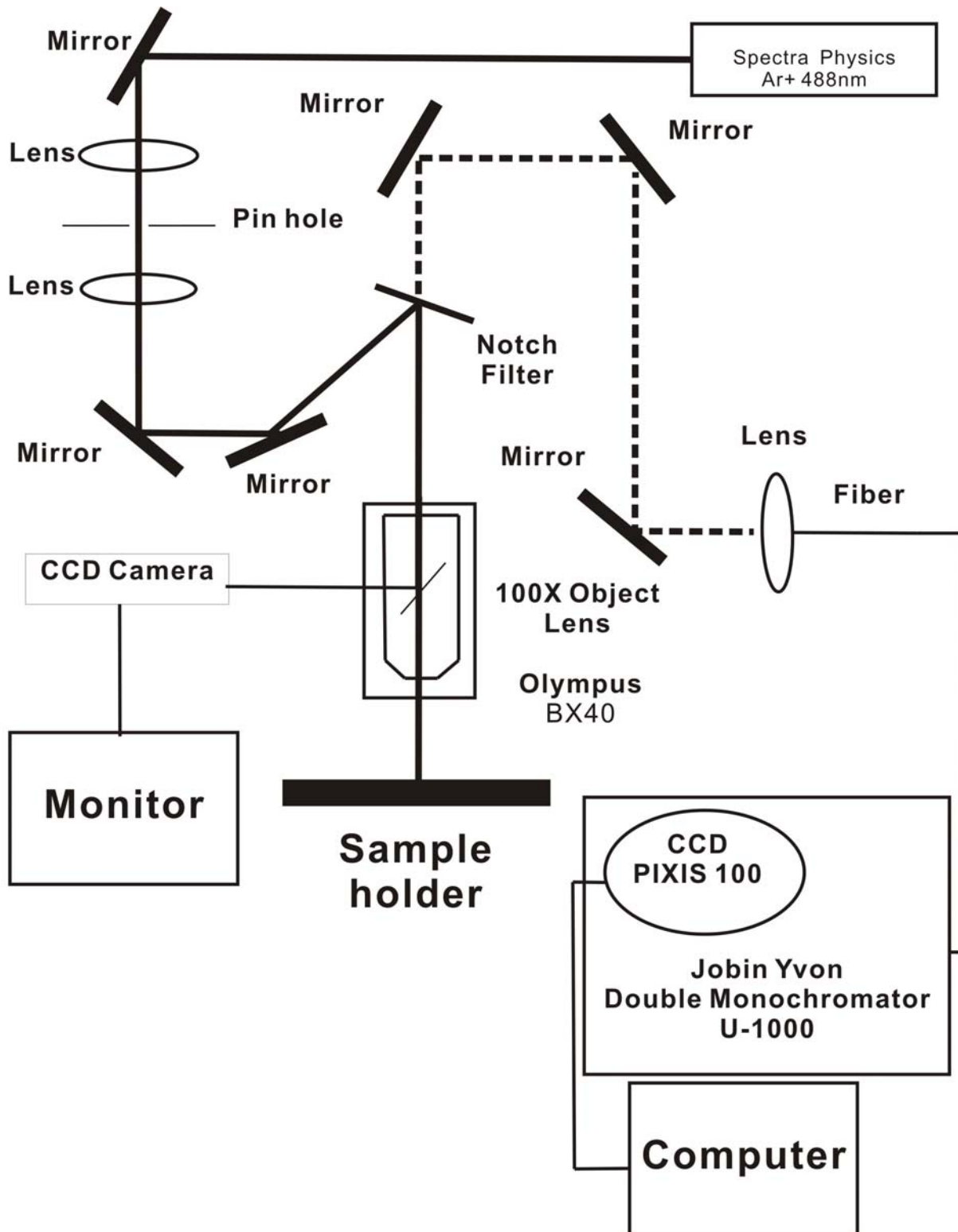


Figure 2-2-1. The schematics of our micro-Raman system

2.3 μ -PL system

The μ -PL system is shown in Figure 2-3-1 that incorporates an optical microscope (Olympus BH2) for probing. A He-Cd laser (KIMMON IK5552R-F) operated at 325/442 nm is the light source. The laser beam is reflected by the mirror and then incident into the system. The beam through the beam splitter and focused by a long working distance near-IR objective lens (Mitutoyo 50X, N.A. =0.42) onto the sample. Because the laser elastic scattering is reflected from the sample, we used a 442 nm long-pass filter to selectively pass the luminescence signals. Finally, the signals are coupled into the monochromator (ARC Pro 500) and collected by the InGaAs (EOS IGA-020-E-LN4) detector. As the entrance and exit slits of the monochromator were both set to 2 mm, the spectra resolution was about 3 nm. In this system, we used a lock-in amplifier to increase the signal to noise (S/N) ratio. The amplified signals were sent to a computer for data processing and analyzing.

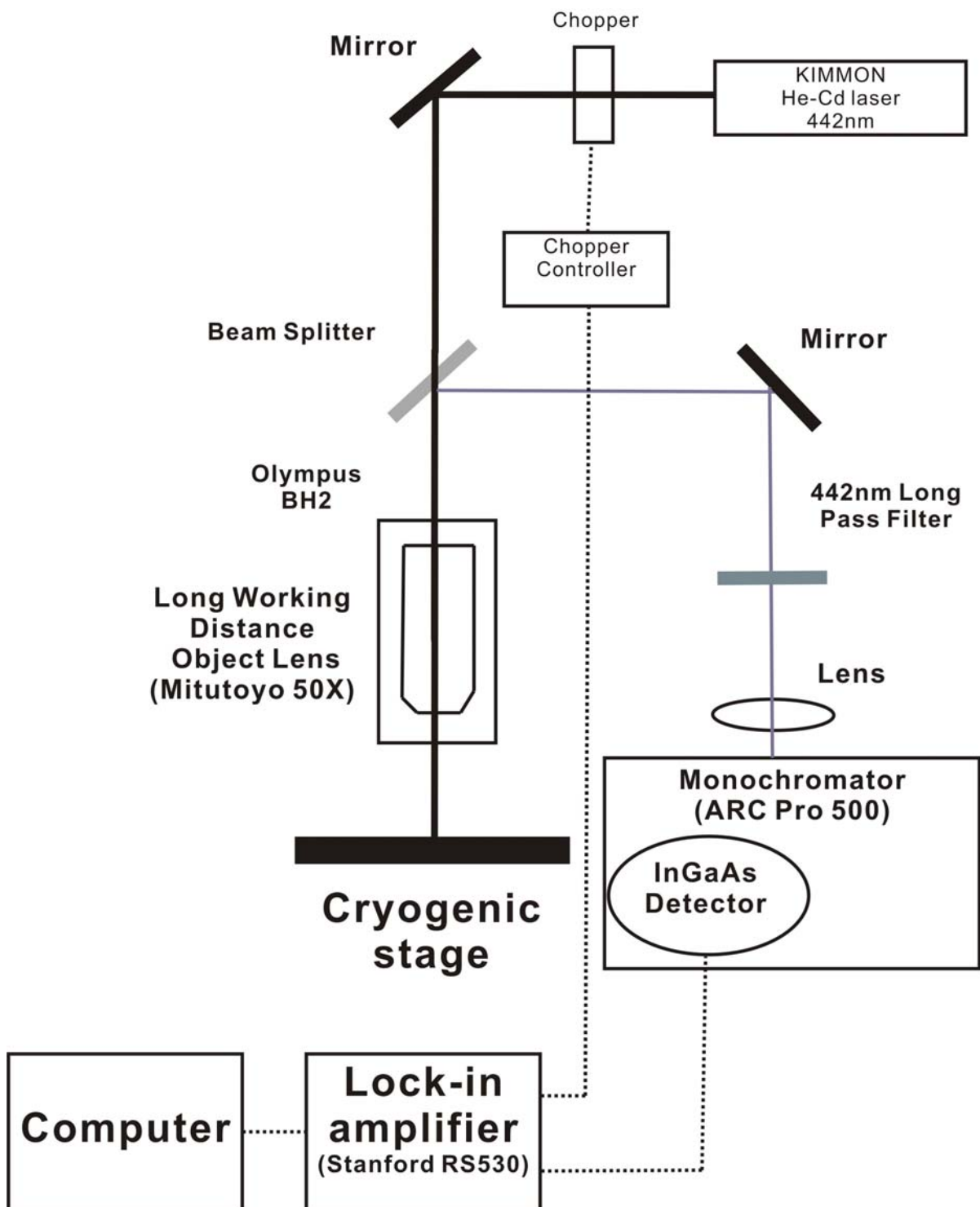


Figure 2-3-1. The schematics of micro-PL system

Chapter 3 Results and Discussion

In this chapter, we will show our X-ray and Raman results first, and then combine these results to estimate the residual strain in samples. Second, we compare the intrinsic strain caused by dot height, and residual thermal strain caused by the different expansion coefficients of GaN and InN. Third, the corresponding PL spectra and the peak energy shift will be discussed. Finally, we will study the GaN capping effect on InN dots.

3.1 The X-ray diffraction results

Figure 3-1-1(a) shows the XRD results of different dot height of InN. These data are aligned with the sapphire (0006) peaks around (41.71°) .

From the reference [11], we know that the diffraction peak of InN (0002) plane is about 31.3° , and that of GaN (0002) plane is about 34.5° . There appear two peaks for GaN, this is because our X-ray target is Cu that has two emissions. Their wavelengths are 1.5405\AA and 1.5443\AA , so that the corresponding diffraction angle (2θ) occurs at 34.46° and 34.56° , respectively. In order to calculate the lattice constant correctly, we also probed the (0004) plane of InN as shown in Figure 3-1-1(b). The angle at about 64.5° is from GaN (2,-1,-1,9) plane for reference [12]. The lattice constant of c-axis is calculated from both results and shown in Table 3-1-1.

From the calculated results, we find that when the InN dots height decreases, the 2θ angle of the (0002) and (0004) planes also decreases. This means that the smaller InN dots experience the larger compressive stress in the a-b plane and the c-axis lattice constant is under tensile strain. We will compare this tendency with the Raman results in the next section.

From the XRD data, we determine the actual c-axis lattice of InN dots of different height. The strain of InN dot is then defined as follows,

$$e_{zz} = \frac{c_{dot} - c_{bulk(relax)}}{c_{bulk(relax)}} \quad (1)$$

where c is the lattice constant along c-axis, the negative strain means the tensile stress and the positive strain means the compressive stress.

In order to determine the strain in InN dot, we must know the c-axis lattice constant of strain-free InN bulk, though it is not well known yet. From the recent researches, the range of the relaxed c-axis lattice constant of InN is 5.7033Å~5.709Å [13, 14]. Hence, we use the extreme values of lattice constant to estimate the strain of InN dot. The results are shown in Table 3-1-1. From the calculated results, the strain of InN dot is compressive, but InN epilayer is under the tensile stress and not strain-free.

These are consistent with recent report of InN [14-15] by Lozano *et al.* They analyzed the strain on InN quantum dots by transmission electron microscopy [14]. The changes in the in-plane lattice parameter of

uncapped InN QD have been measured using moiré fringe analysis. The uncapped InN QDs are mostly relaxed with the plastic relaxation $\delta \approx 97\%$ for dot height of 12 nm. The plastic relaxation δ and the residual strain of our uncapped InN dots were also calculated in Table 3-1-1. It is obvious that the residual strain is really small. If the relaxed lattice constant is 5.7033\AA , the residual strain is almost the same as that in reference [15].

The FWHM tendency of X-ray shows that the 28 nm dot has better quality than others. This may be due to that 28 nm dots experience the smallest compressive strain.



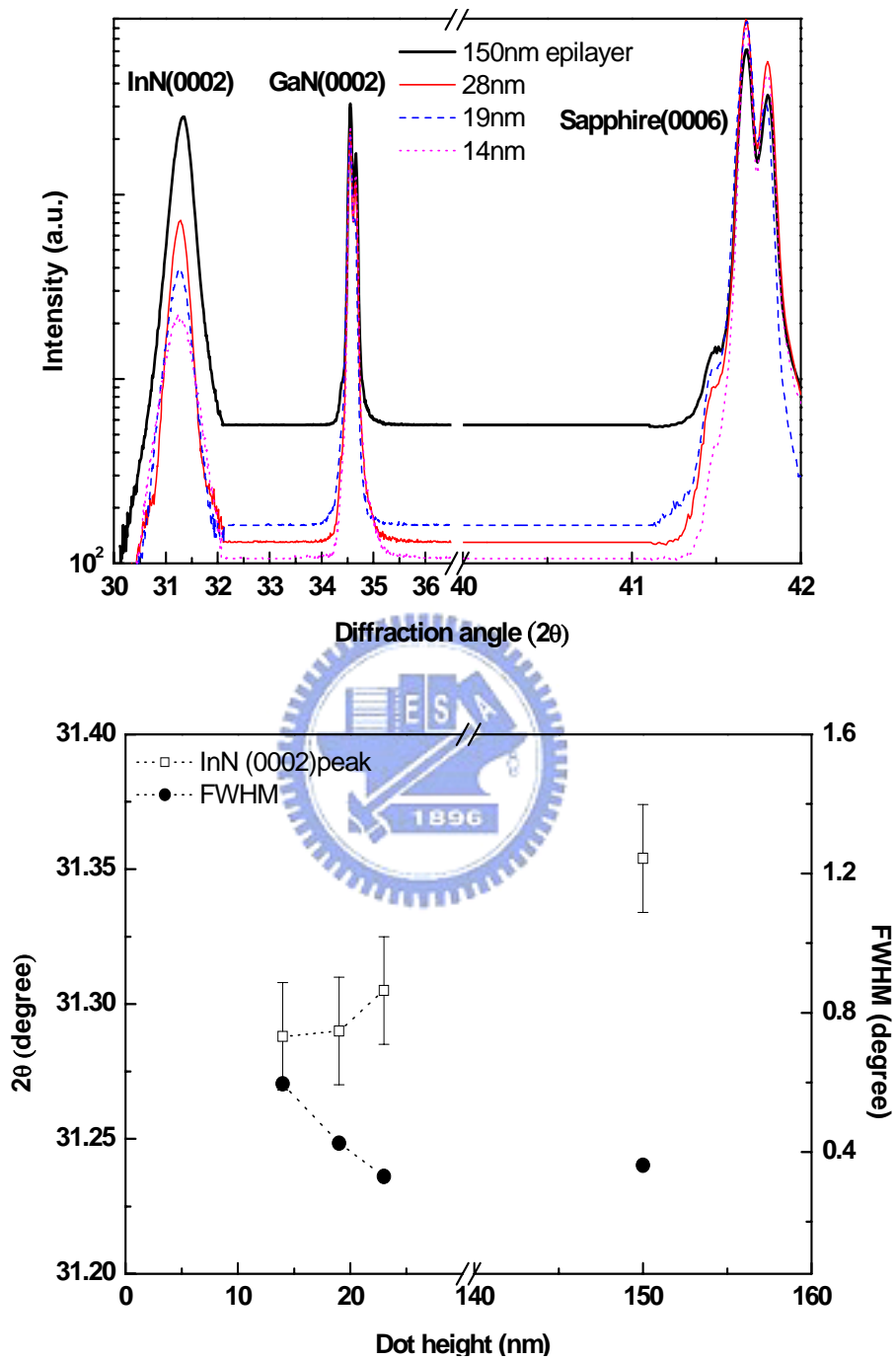


Figure 3-1-1 (a). The XRD and FWHM pattern of the (0002) InN epilayer and dots grown at 700°C (the error bar of FWHM is included in the plot)

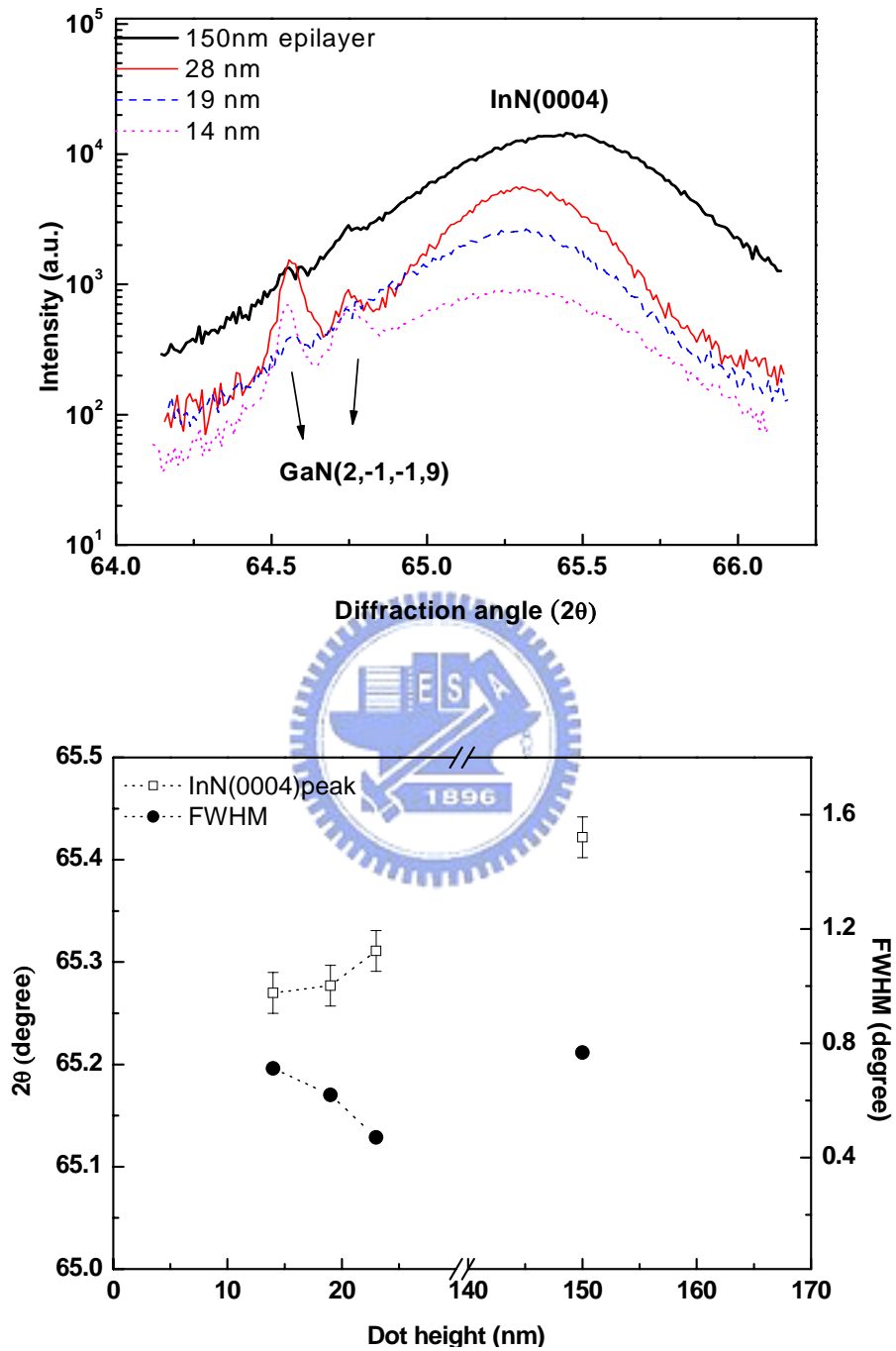


Figure 3-1-1 (b). The XRD and FWHM pattern of the (0004) InN epilayer and dots grown at 700^oC (the error bar of FWHM is included in the plot)

	Lattice constant (Å)	Strain (e_{zz})(%) with respect to 5.7033 Å	Strain (e_{zz})(%) with respect to 5.709 Å
Epilayer 150nm	5.7013	-0.0351	-0.1349
Dot height 28nm	5.7100	0.1175	0.0175
Dot height 19nm	5.7126	0.1631	0.0631
Dot height 14nm	5.7130	0.1701	0.0700

	Strain (e_{zz})(%) with respect to 5.709Å	Plastic relaxation (δ) (%)	Residual strain (1- δ) (%)
Epilayer 150nm	-0.1349		
Dot height 28nm	0.0175	99.81	0.19
Dot height 19nm	0.0631	99.32	0.68
Dot height 14nm	0.0700	99.23	0.76

	Strain (e_{zz})(%) with respect to 5.7033Å	Plastic relaxation (δ) (%)	Residual strain (1- δ) (%)
Epilayer 150nm	-0.0351		
Dot height 28nm	0.1175	98.72	1.28
Dot height 19nm	0.1631	98.22	1.78
Dot height 14nm	0.1701	98.15	1.85

Table 3-1-1. The lattice constant and the calculated strain and plastic relaxation of InN epilayer and dots grown at 700°C

3.2 The Raman scattering of uncapped InN (dots)

The μ -Raman spectra of InN epilayer and nano-dots with different dot height are shown in Figure 3-2-1.

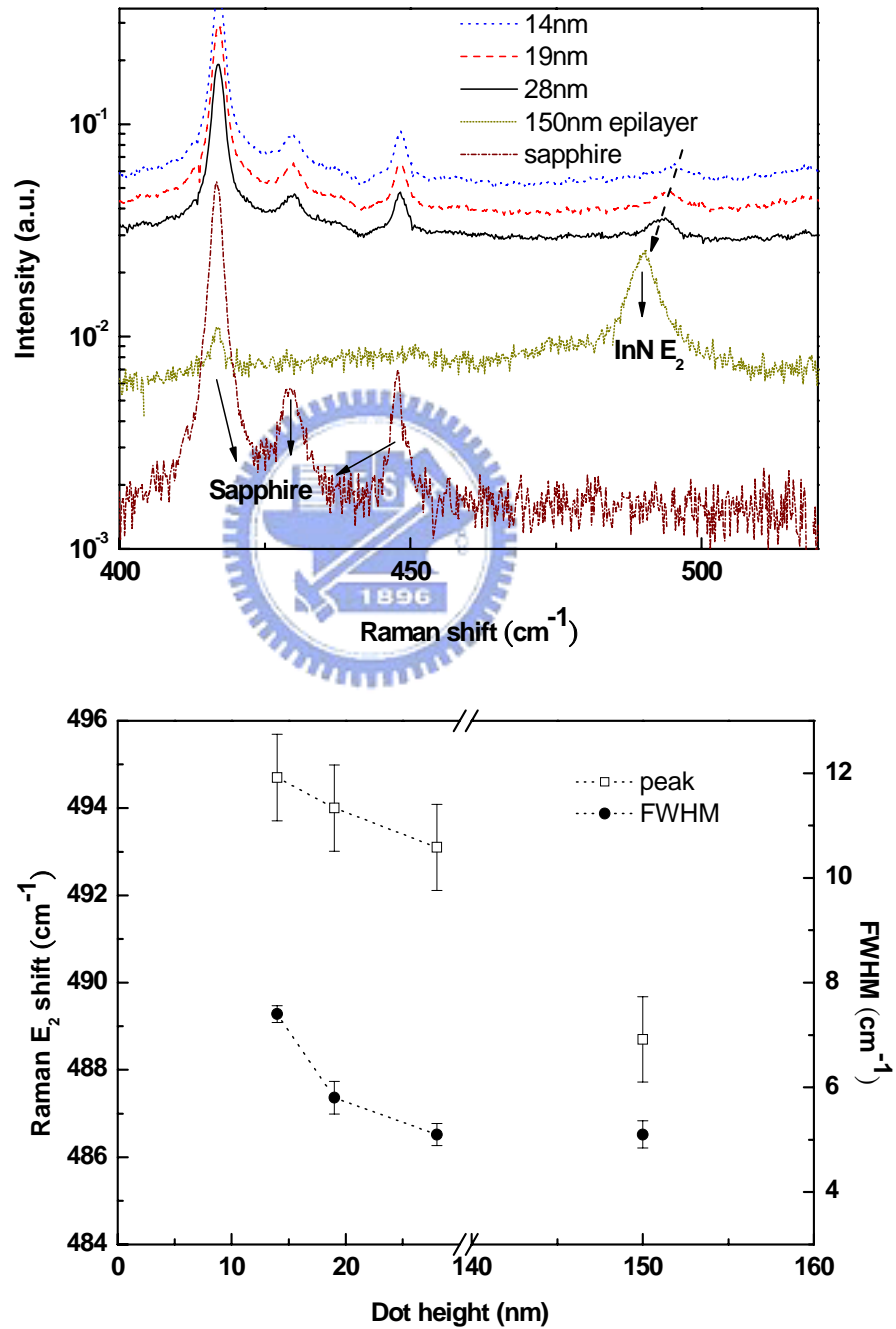


Figure 3-2-1. The Raman spectra, shift and FWHM of the InN epilayer and dots grown at 700°C

The peaks at 418 cm^{-1} , 430 cm^{-1} , and 448 cm^{-1} , are the signals from sapphire, so that only the peak at 493 cm^{-1} is from InN E_2 mode. As the dot height decreases, this Raman mode shift increases.

From this Figure, we can see that the Raman E_2 mode of InN dots is shifted more than 5cm^{-1} with respect to that of epilayer. There are two possible causes for this behavior, one is the compressive stress and the other is the formation of InGaN alloy. By comparing with X-ray results, this large blue shift in InN dots is more likely due to the compressive stress. The FWHM behavior shows that the 28 nm InN dots quality is also better than others, similar to X-ray results. From the X-ray and μ -Raman measurements, we investigate the stress effect on InN dots and examine our results with published data.

Up to now, we have considered the strain of InN dot. In the following, we will discuss the correlation between Raman shifts and strains. Because our epilayer sample is not strain-free, we do not have a standard strain-free frequency of the E_2 mode. Hence, we use the method from the reference [13], to determine the strain-free frequency of E_2 mode in our system. Then, we use this strain-free frequency to check the accuracy of the calculated strain. The Poisson ratio ($\frac{e_{zz}}{e_{xx}}=0.72$) we used to calculate the strain in the a-b plane is the same as that in reference [13]. The results are shown in Figure 3-2-2

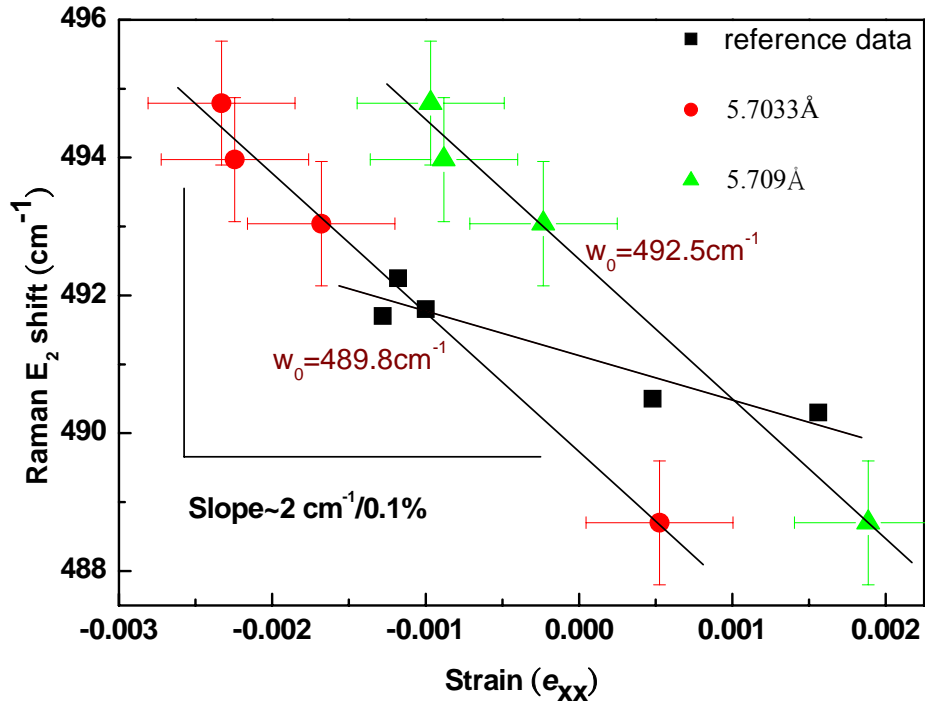


Figure 3-2-2. The strain-free frequency of E_2 mode for our samples

We can see that the strain-free E_2 mode frequency for our samples is between 489.8 cm^{-1} and 492.5 cm^{-1} that depends on the relaxed c-axis lattice constant. Our results are consistent with the published data presented in Table 1-2 that shows a range from 488 cm^{-1} to 494 cm^{-1} for various samples.

Up to now, we have studied the E_2 modes of InN under the compressive strain and predicted the strain-free condition. Whether the strain is intrinsic or residual will be addressed in the next section.

3.3 The residual thermal strain of InN dots due to growth temperature

In this section, we will consider the effect of residual thermal strain [16]. The growth temperature we used is 625°C, 650°C, 700°C, but the range of dot height is from 28 nm to 32 nm. The difference of the thermal expansion coefficient between film and substrate is the main cause for the residual thermal strain, the expansion coefficient of GaN and InN are $5.11 \times 10^{-6} \text{ K}^{-1}$ and $3.8 \times 10^{-6} \text{ K}^{-1}$, respectively [17]. As the growth temperature increases, the residual thermal strain ε (%) also increases [16]. Hence, we used X-ray diffraction and the Raman scattering (E_2 mode shift) to investigate this phenomenon and shows in Figures 3-3-1 and 3-3-2. The corresponding c-axis lattice constant and residual thermal strain is calculated in Table 3-3-1. In order to double check the E_2 mode strain-free frequency, we combine the calculated residual thermal strain and the Raman E_2 mode shift (the same as that in section 3-2) that shown in Figure 3-3-3. From this Figure, we can use the linear interpolation to find the E_2 mode strain-free frequency ($\sim 490.3 \text{ cm}^{-1}$). This frequency is almost the same as that shown in section 3-2 when the relaxed lattice constant is 5.7033Å.

Comparing the thermal strain from X-ray results and that due to the difference of the thermal expansion coefficient between film and substrate

(ideal), we notice that they are similar. This reflects that the calculated thermal strain and the E_2 strain-free frequency are reasonable.

It is clear that both the Raman shift and the residual thermal strain increase with the growth temperature. In section 3-2, when the strain changes by 0.1%, for different dot height, the Raman E_2 mode shift will also changes by $\sim 2 \text{ cm}^{-1}$. In this part, when the strain changes by 0.1%, for different growth temperature, the Raman E_2 mode will shift changes by $\sim 3 \text{ cm}^{-1}$. Therefore, the Raman E_2 mode shift is more sensitive to thermally induced strain than dot height induced strain.



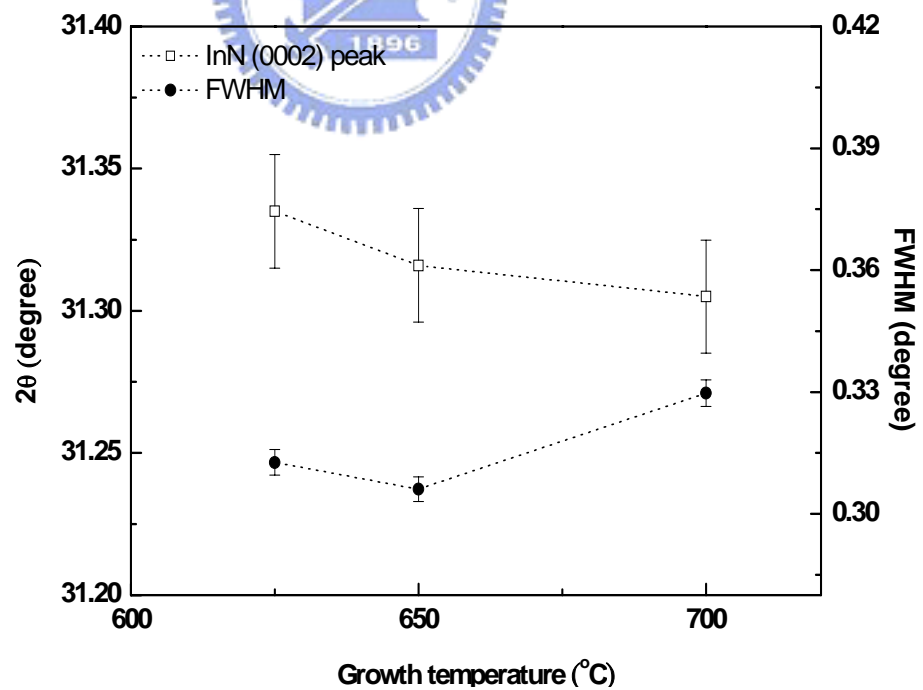
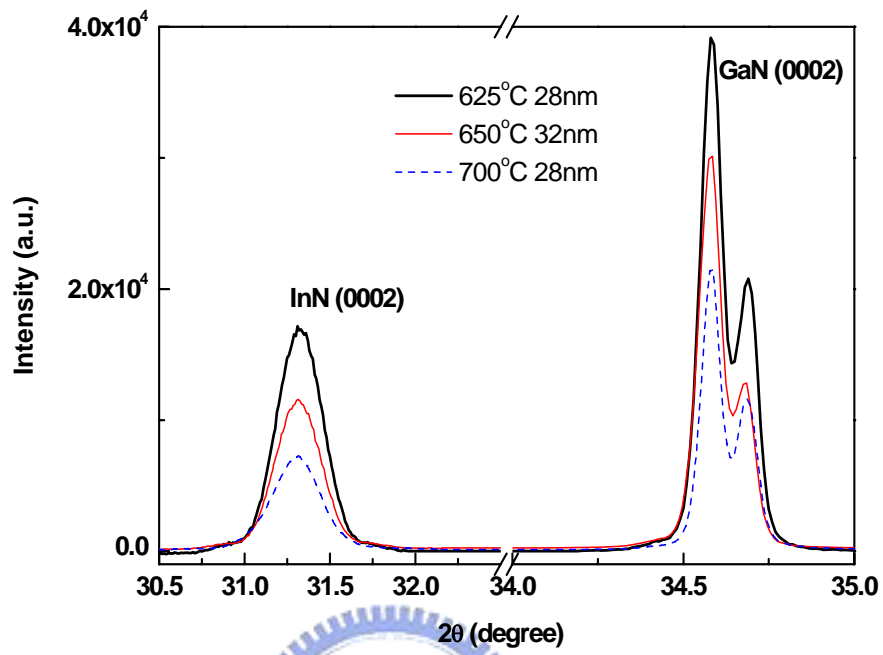


Figure 3-3-1. The XRD and FWHM pattern of the InN dots grown at different temperature.

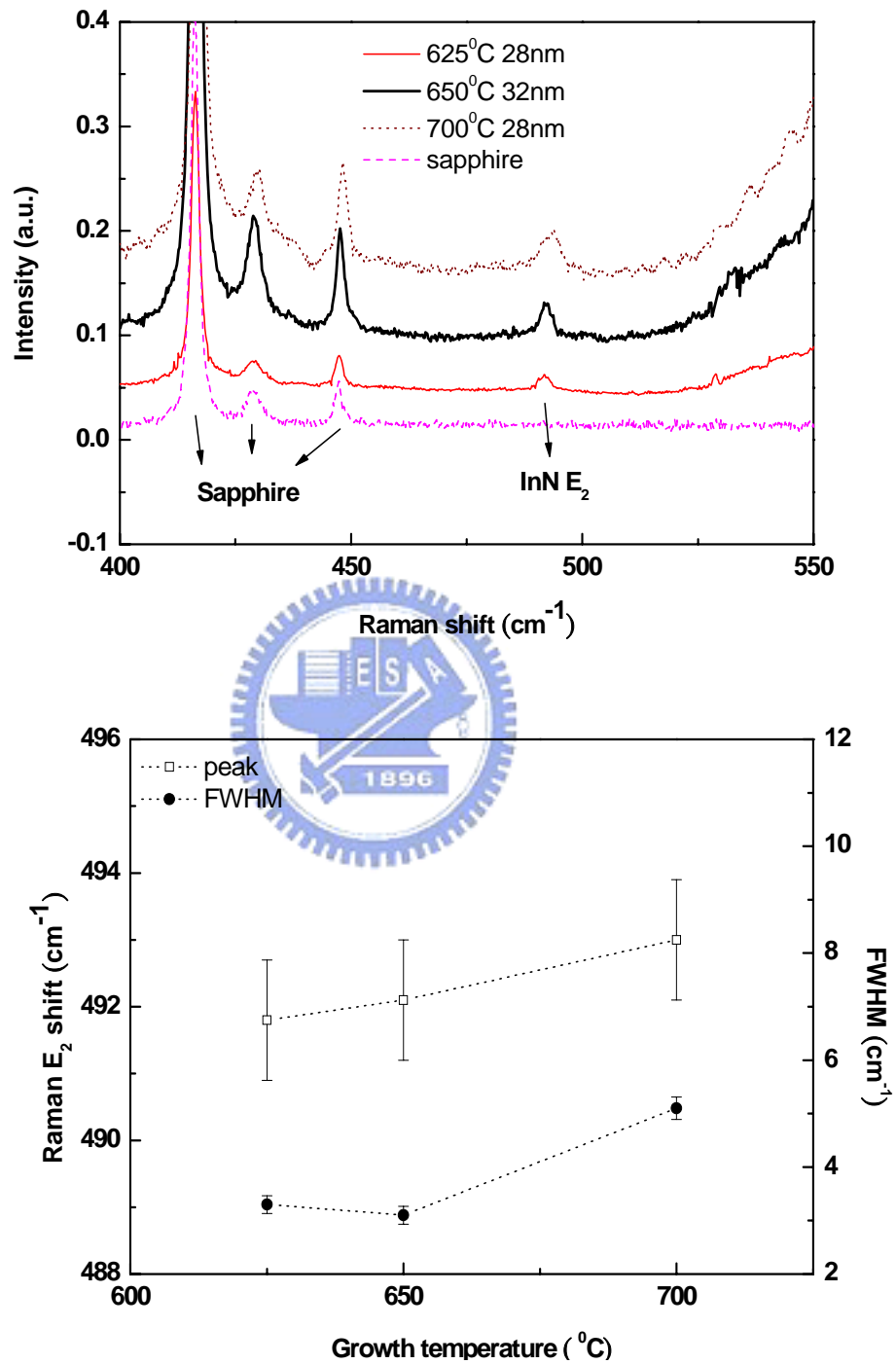


Figure 3-3-2. The Raman shift and FWHM of the InN dots grown at different temperature

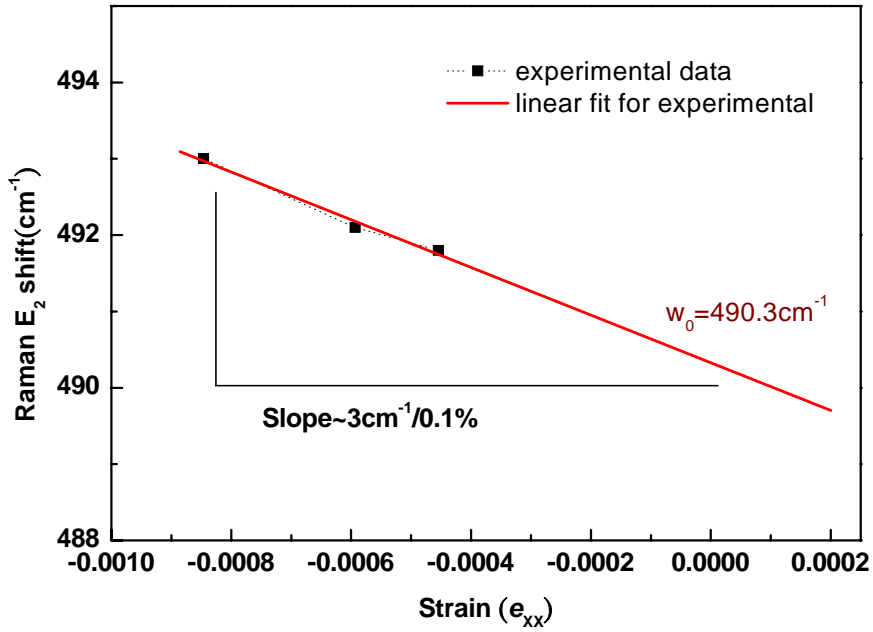


Figure 3-3-3. The strain-free frequency of E₂ mode for different growth temperature

(with respect to 5.7033 Å)

Growth temperature (°C)	Lattice constant (Å)	Thermal strain (%) with respect to 5.7033 Å	Ideal thermal strain (%)	Raman E ₂ shift (cm ⁻¹)
625°C Dot height 28nm	5.7069 Å	0.0631	0.0786	491.8±0.9
650°C Dot height 32nm	5.7080 Å	0.0824	0.0819	492.1±0.9
700°C Dot height 28nm	5.7100 Å	0.1175	0.0885	493.0±0.9

Table 3-3-1. Residual thermal strain and c-axis lattice constant of InN dots grown at different temperature

3.4 The PL results of InN dots

In this section, the PL characteristics of uncapped InN dots with different height were measured as shown in Figure 3-4-1. The strong luminescence is due to the band to band transition, according to reports [1-5]. Obviously, the band gap of InN dots shows a blue shift from 53 meV to 60 meV with respect to the epilayer. Though, a few effects may change the band gap energy of III-nitride quantum dots, we will focus on the strain and confinement effects to account for the energy shift between InN epilayer and dots.

The PL FWHM shows that the InN quality of 28 nm dot height is better than others. It is similar to that of X-ray and μ -Raman results. This indicates that the smallest compressive strain is present in 28 nm quantum dots.

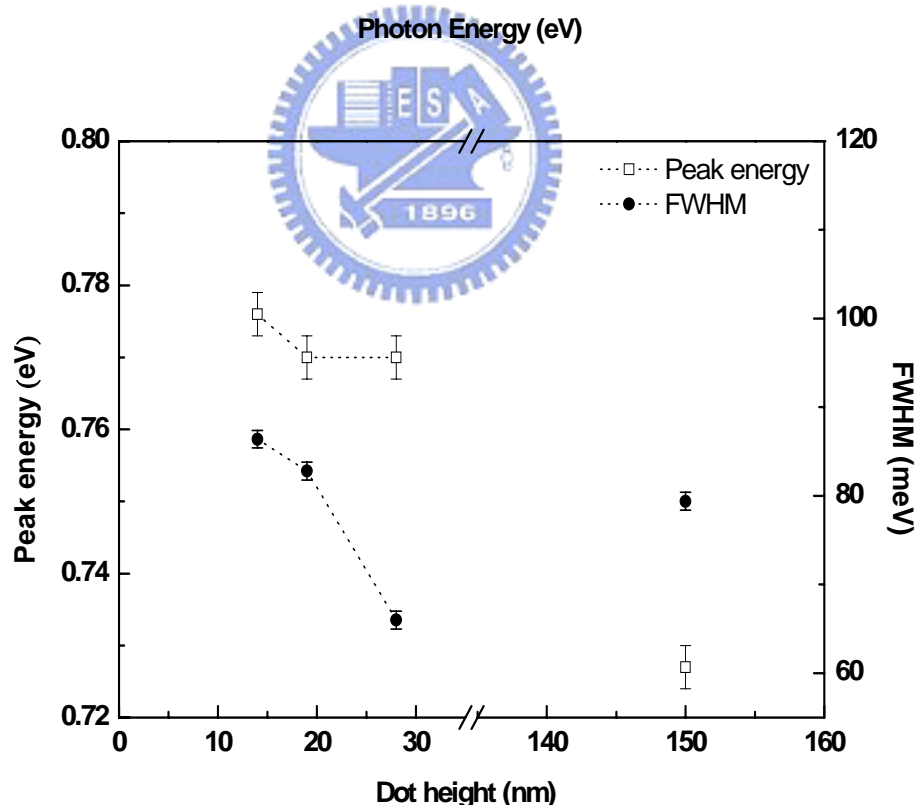
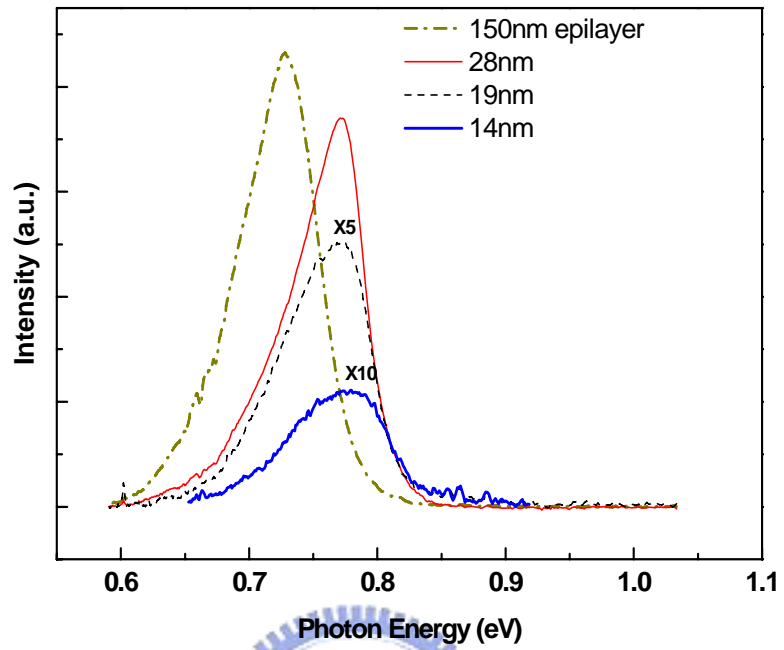


Figure 3-4-1. The PL spectra, peak position and FWHM of InN epilayer and dots (grown at 700⁰C)

3.4.1 Quantum confinement effect

The quantum confinement effect can shift the band gap of a bulk semiconductor to higher energy. This shift, called the confinement energy, depends on the size and shape as well as the material properties of both quantum dots and surrounding matrix. Assuming that an electron is in a rectangular box with infinite barrier, the confinement energy of the ground state is given by,

$$E = \frac{h^2}{8} \left(\frac{1}{m_x d_x^2} + \frac{1}{m_y d_y^2} + \frac{1}{m_z d_z^2} \right) \quad (1)$$

where d_j ($j=x, y$ and z) is the dimension of the box and m_j is the electron mass in j direction. Since InN dots in our samples are disk-like, the confinement energy is simplified to

$$E = \frac{h^2}{8} \frac{1}{m_z d_z^2} \quad (2)$$

The reduced mass is used for calculation,

$$\frac{1}{m_z} = \frac{1}{m_{e,z}} + \frac{1}{m_{h,z}} \quad (3)$$

where $m_{e,z}$ and $m_{h,z}$ are, respectively, the effective masses of the electrons and holes in III-nitride along the z -direction. Although the effective masses of the electrons and holes in InN are not exactly determined, we adopted $m_{h,z} \approx 0.1m_0$ and $m_{e,z} \approx 0.042m_0 \sim 0.07m_0$ to estimate the confinement energy [18]. The calculated results for different dot height are shown in Table 3-4-1. Obviously, they cannot account for the total blue shift of our experimental results. Thus, other effects should be taken into account.



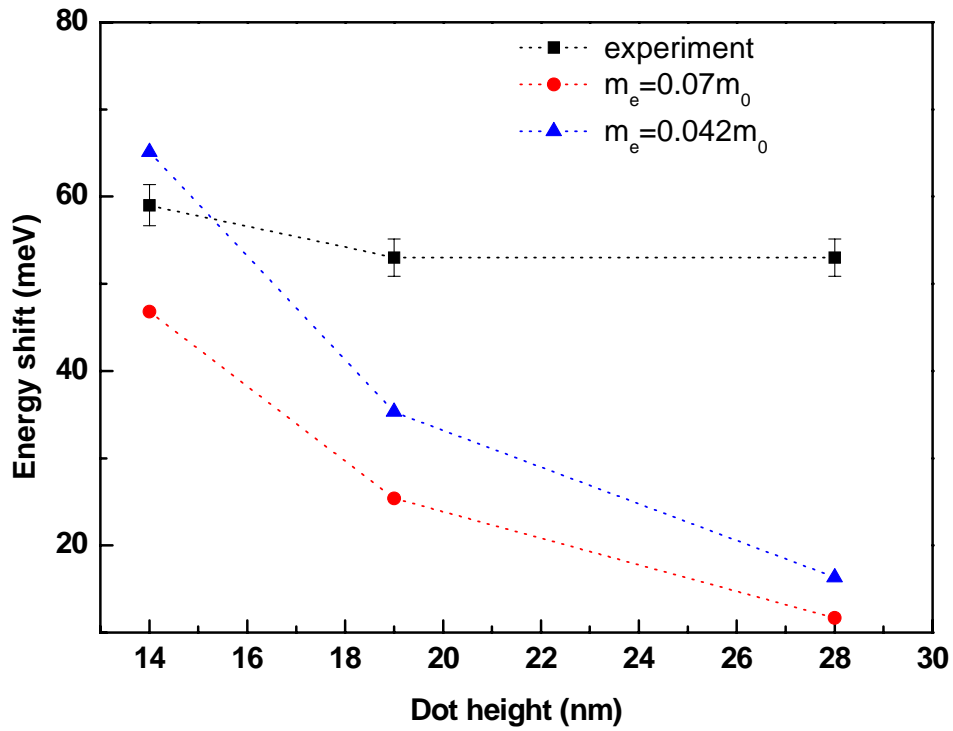


Figure 3-4-2. The energy shift due to confinement effect

	Peak energy (eV)	Blue shift (meV)	Confinement energy (meV) for $m_e=0.07m_0$	Confinement energy (meV) for $m_e=0.042m_0$
Epilayer 150nm	0.727			
Dot height 28nm	0.770	53 ± 3	11.7	16.3
Dot height 19nm	0.770	53 ± 3	25.4	35.3
Dot height 14nm	0.776	59 ± 3	46.8	65.1

Table 3-4-1. Calculated confinement energy of the InN dots with different effective mass of electron

3.4.2 Strain effect

In this section, we will consider the energy shift due to the strain as revealed from previous XRD results. In reference [12], the relationship between PL peak energy shift and the lattice constant change can be expressed as the following,

$$E = \alpha\left(\frac{\Delta l}{l}\right) + \beta\left(\frac{\Delta l}{l}\right)^2 \quad (1)$$

where α and β are the relative constants and given in Table 3-4-2.

	α (eV)	β (eV)
InN		
$\Gamma_v - \Gamma_c$	-12	49
$\Gamma_v - K_c$	-0.63	-11
$\Gamma_v - M_c$	-16	-44
$\Gamma_v - A_c$	-12	15
$\Gamma_v - L_c$	-8.5	-6.5
$\Gamma_v - H_c$	-15	-49

Table 3-4-2. The coefficients of relative energy shift

Hence, the energy shift from the c-axis length change is calculated for different dot height as shown in Table 3-4-3. They are also shown in Figure 3-4-3 for comparison.

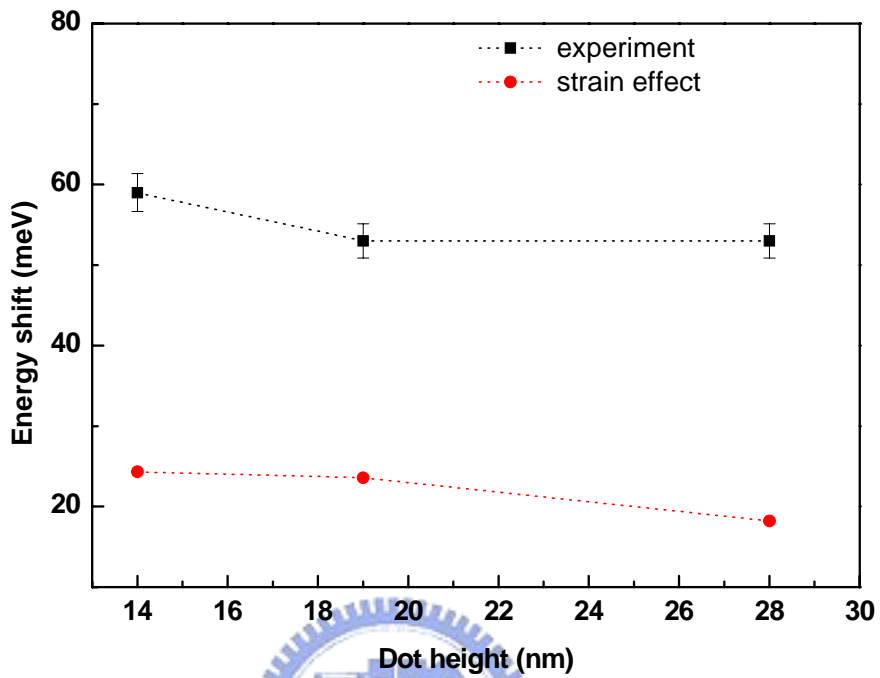


Figure 3-4-3. Comparison the experimental energy shift with strain effect

	Peak energy (eV)	Blue shift (meV)	$\frac{\Delta l}{l}$ (%)	Strain induced blue shift (meV) (estimated by XRD)
Epilayer 150nm	0.727			
Dot height 28nm	0.770	53 ± 3	0.153	18.2
Dot height 19nm	0.770	53 ± 3	0.198	23.6
Dot height 14nm	0.776	59 ± 3	0.205	24.3

Table 3-4-3. Calculated energy shift from strain of the InN dots grown at 700°C

Either the confinement or strain effects cannot account for the experimental results. By combining the confinement and strain effects, the general trend with the experiment results is reasonable as shown in Figure 3-4-4.

Hence, we believe that both the confinement and strain are dominant effects in our samples, even though other effects such as the carrier concentration [19] and piezoelectric effect [20] that could cause the blue shift. From [19], the optical band edge covers a wide range from 0.7eV to about 1.7 eV when free electron concentrations range from $1.7 \times 10^{18} \text{ cm}^{-3}$ to $4.5 \times 10^{18} \text{ cm}^{-3}$. If the free electron concentration is the only effect that causes this blue shift from 53 meV to 60 meV in our samples, the free electron concentration of InN dot should be five times larger than InN player [19]. Because we cannot measure the free electron concentration exactly in our nano-dot samples, it is we assumed that the free electron concentration is the same in both InN epilayer and InN nano-dot.

When the InN dot experiences the compressive strain, there will be induced some piezoelectric polarization [21]. Hence, the red shift of the energy is given by [22]

$$\Delta E = 24 \left(\frac{2}{3\pi} \right)^6 \frac{e^2 \varepsilon_z^2 m^* d^4}{\hbar^2} \quad (1)$$

where d is the dot height, ε_z is the component of the piezoelectric field in

the z direction and m^* is the effective mass. The energy red shift by the induced piezoelectric field is about 150meV estimated by eq (1) for the dot height is 19 nm, the electric field is $3.45 \times 10^7 \text{ Vm}^{-1}$ and $m_e=0.042m_0$, $m_h=0.1m_0$. In our results, we did not see such large energy shift, so that the piezoelectric effect is not considered here.

The large deviation at small dot height from calculation may be due to the nonuniform dot height distribution. Thus, we did not observe strong confinement effect induced blue shift.

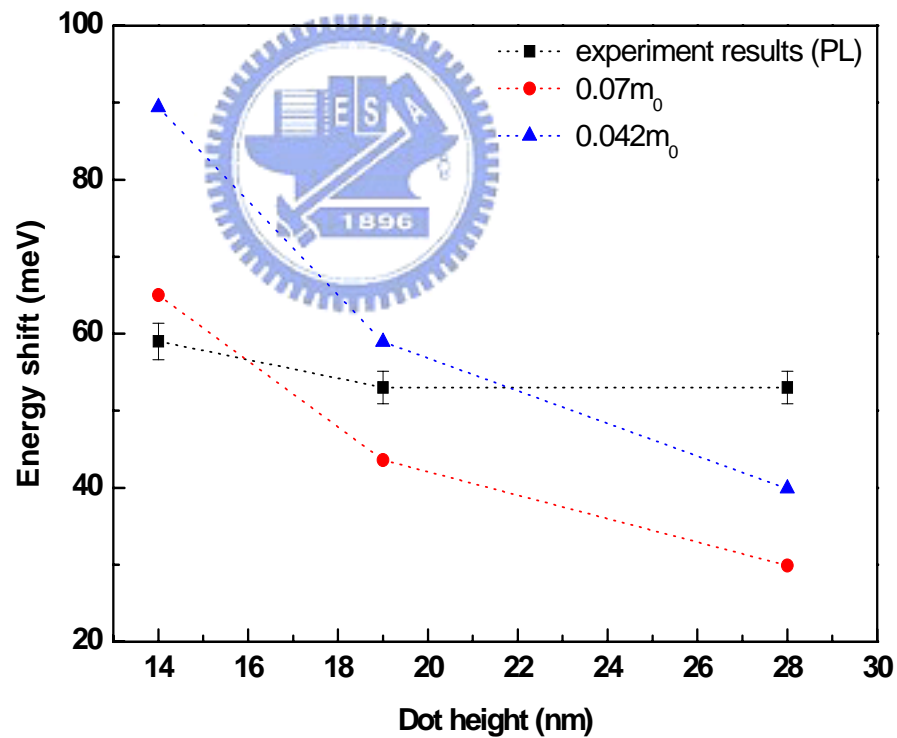
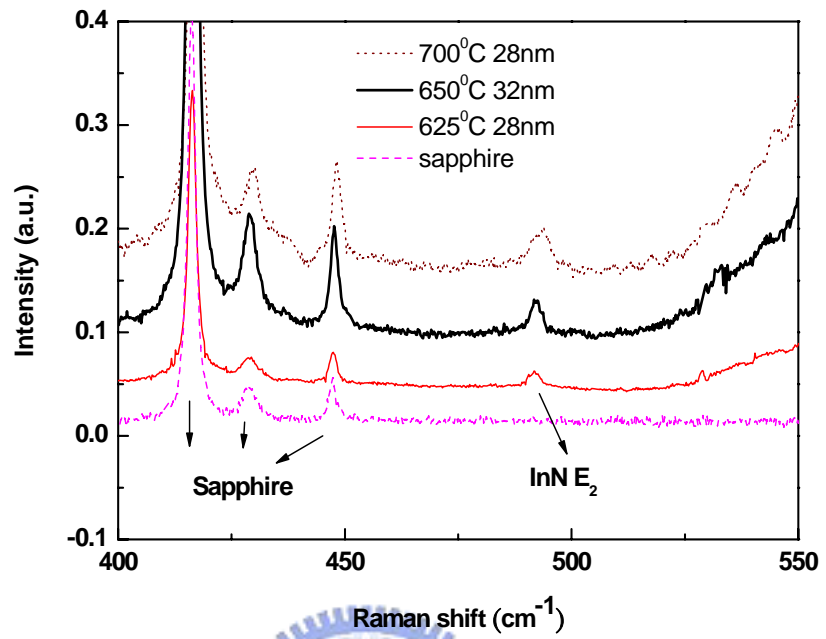


Figure 3-4-4. Comparison of the experiment energy shift with combined confinement and strain effects

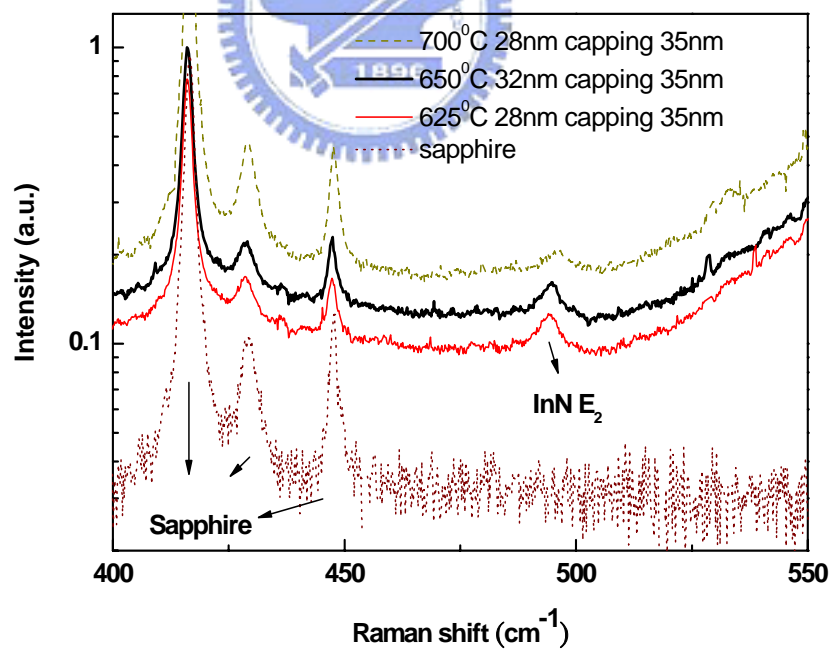
3.5 The capping effect

Up to now, we have presented the optical properties of uncapped InN dots. In this section, we will study the GaN capping effect on InN dots. Figure 3-5-1 (a and b) shows the Raman results of InN dots grown at different temperature with and without capping of 35 nm GaN.

We see that the InN E_2 peak is shifted to high frequency by about 2~3 cm^{-1} . Hideaki Saito indicated that when the surface dots are covered by a cap layer, the compressive stress will be induced [15, 23]. Hence the Raman shift increases. Because the c-axis lattice constant changes after capping [23], it is not appropriate to use X-ray diffraction to estimate the strain of a-b plane as before. Then, we used a linear approximation from the Raman E_2 shift to estimate the strain of a-b plane between uncapped and capped InN dots. The estimated results are shown in Table 3-5-1 with the corresponding experimental results. After capping 35 nm GaN, we can see that the compressive strain increases by about 0.09% (the plastic relaxation δ decreases about 1%) and the FWHM also increases by about 1.3 cm^{-1} . When the InN dots experience the smaller compressive strain, they have better quality. This tendency is consistent with X-ray and Raman results.



(a)



(b)

Figure 3-5-1. The Raman shift of InN dots (a) without capping (b) with capping 35nm GaN

	Raman E₂ mode shift (cm⁻¹)	FWHM (cm⁻¹)	Strain (%) with respect to 5.7033Å
dot (625°C) (28nm)	491.8±0.9	3.3±0.2	0.0631
capping (35nm)	494.1±0.9	5.0±0.2	0.1528
dot (650°C) (32nm)	492.1±0.9	3.1±0.2	0.0824
capping (35nm)	494.4±0.9	4.8±0.2	0.1645
dot (700°C) (28nm)	493.0±0.9	5.1±0.2	0.1175
capping (35nm)	495.8±0.9	5.7±0.2	0.2267

Table 3-5-1. The Raman shift, FWHM and the strain of the capped and uncapped InN dots

Chapter 4 Conclusions

In this thesis, we have utilized X-ray diffraction and μ -Raman and μ -PL methods to characterize the strain of InN epilayer and dots of different dot height grown at different temperature with and without capping .

As the dot height decreases or the growth temperature increase, the Raman E_2 mode shift increases and the 2θ angle of the (0002) and (0004) planes also decreases. This means that the InN dots experience the larger compressive stress in the a-b plane so that the c-axis lattice constant is under tensile strain. We also checked the effect due to the growth temperature and dot height. From the Raman shift frequency of E_2 and the calculated strain, we can anticipate the strain-free frequency by interpolation. The estimated results for the strain of both InN epilayer and dots are reasonable by using optical characterizations.

For the blue shift in PL spectra with decreasing dot height in our samples, we believe that both the confinement and strain effects are important in addition to other effects. Finally, we studied the GaN capping effect on InN dots and showed that when the surface dots are covered by a cap layer, the compressive stress will be induced on the a-b plane.

Reference

- [1] V. Yu. Davydov, A. A. Klochikhin, R. P. Seisyan, V. V. Emtsev, S. V. Ivanov, F. Bechstedt, J. Furthmüller, H. Harima, A. V. Mudryi, J. Aderhold, O. Semchinova, and J. Graul, *Phys. Stat. Solidi (b)*, **229**(3), R1 (2002). V. Yu. Davydov, A. A. Klochikhin, V. V. Emtsev, S. V. Ivanov, V. V. Vekshin, F. Bechstedt, J. Furthmüller, H. Harima, A. V. Mudryi, A. Hashimoto, A. Yamamoto, J. Aderhold, J. Graul, and E. E. Haller, *Phys. Stat. Sol.(b)*, **230**(2), R4 (2002).
- [2] J. Wu, W. Walukiewicz, K. M. Yu, J. W. Ager III, E. E. Haller, H. Lu, W. J. Schaff, Y. Saito, and Y. Nanishi, *Appl. Phys. Lett.* **80**, 3967 (2002). J. Wu, W. Walukiewicz, K. M. Yu, J. W. Ager III, E. E. Haller, Hai Lu, and William J. Schaff, *Appl. Phys. Lett.* **80**, 4741 (2002).
- [3] M. Hori, K. Kano, T. Yamaguchi, Y. Saito, T. Araki, Y. Nanishi, N. Teraguchi, and A. Suzuki, *Phys. Stat. Sol.(b)*. (b) **234**, 750 (2002).
- [4] For a review, see M. Leroux and B. Gil in *Gallium Nitride and Related Semiconductors* edited by J. H. Edgar, S. Strite, I. Akasaki, H. Amano and C. Wetzel, EMIS DATA REVIEWS SERIES 23, INSPEC publications ISBN 0 85296 953 8 (1999), 117.
- [5] F. Bechstedt and J. Furthmüller, *Journal of Crystal Growth* **246**, 315, (2002).
- [6] Z, G, Qian, W, Z, Shen, H, Ogawa and Q, X, Guo *J. Phys.: Condens. Matter* **16** (2004) R381–R414
- [7] Shen S. C. 2002 *Semiconductor Spectroscopy and Optical Properties* (Beijing: Scientific)
- [8] Cheng G X 2001 *Raman and Brillouin Scattering — Principles and Applications* (Beijing: Scientific)
- [9] M. Caordona and G. Guntherodt, editors. *Light Scattering in Solid II:*

Basic Concepts and Instrumentation, volume 50 of Topics in Applied Physics.

- [10] Ashraful Ghani Bhuiyan, Akihiro Hashimoto, and Akio Yamamoto, J. Appl. Phys. **94**, 2779 (2003).
- [11] Yeh. C et al. Phys. Rev. B46, 10086(1992)
- [12] Christensen, N.E., Gorczyca, I. Phys. Rev. B50, 4397(1994)
- [13] V. Darakchieva, P. P. Paskov, E. Valcheva, T. Paskova, and B. Monemar, Appl. Phys. Lett. **84**, 3636 (2004)
- [14] Kwiseon Kim, Walter R. L. Lambrecht, and Benjamin Segall, Phys. Rev. B53, 16310(1996)
- [15] J. G. Lozano, A. M. Sanchez Appl. Phys. Lett. **88**, 151913 (2006)
- [16] E. Kurimoto, H. Harima, A. Hashimoto, and A. Yamamoto, Phys. Status Solidi B **228**, 1(2001).
- [17] Maciej Dems and Włodzimierz Nakwaski, Semicond. Sci. Technol. **18** 733–737 (2003)
- [18] J. Wu, W. Walukiewicz, W. Shan, K. M. Yu, J. W. Ager, Phys. Rev. B66, 201403 (2002)
- [19] J. Wu and W. Walukiewicz, Appl. Phys. Lett. **84**, 2805 (2004)
- [20] S. Sanguinetti, M. Gurioli, E. Grilli, and M. Guzzi, Appl. Phys. Lett. 77, 1982 (2000)
- [21] O Ambacher, J. Phys D: Appl. Phys. 312659 (1998)
- [22] Mark Fox 2001 Optical Properties of Solids p.131 (OXFORD)
- [23] Hideaki Saito, Kenichi Nishi, and Shigeo Sugou, Appl. Phys. Lett. 73, 2742 (1998)